Investigating the Composition of the Metal Dimer Site in Chabazite for Direct Methane-to-Methanol Conversion

THE JOURNAL OF PHYSICAL CHEMISTRY C
A JOURNAL OF THE AMERICAN CHEMICAL SOCIETY

pubs.acs.org/JPCC
Article

Investigating the Composition of the Metal Dimer Site in Chabazite for Direct Methane-to-Methanol Conversion

Published as part of The Journal of Physical Chemistry C virtual special issue "Jens K. Nørskov Festschrift".

Unni Engedahl, Astrid Boje, Henrik Ström, Henrik Grönbeck, and Anders Hellman*

Cite This: J. Phys. Chem. C 2024, 128, 3641−3651

Read Online

ACCESS | Metrics & More | Article Recommendations | Supporting Information

ABSTRACT: Methanol is a liquid energy carrier that has the potential to reduce the use of fossil fuels. Industrial production of methanol is currently a multistep high-temperature/high-pressure synthesis route. Direct conversion of methane to methanol under low-temperature and low-pressure conditions is an interesting but challenging alternative, which presently lacks suitable catalysts. Here, the complete reaction cycle for direct methane-to-methanol conversion over transition-metal dimers in the chabazite zeolite is studied by using density functional theory calculations and microkinetic modeling. In particular, a reaction mechanism previously identified for the Cu_2 dimer is explored under dry and wet conditions for dimers composed of Ag, Au, Pd, Ni, Co, Fe, and Zn and the bimetallic dimers AuCu, PdCu, and AuPd. The density-functional-theory-based microkinetic modeling shows that Cu_2, AuPd, and PdCu dimers have reasonable turnover frequencies under technologically relevant conditions. The adsorption energy of atomic oxygen is identified as a descriptor for the reaction landscape as it correlates with the adsorption and transition-state energies of the other reaction intermediates. Using the established scaling relations, a volcano plot of the rate is generated with its apex close to the Cu_2, AuPd, and PdCu dimers.

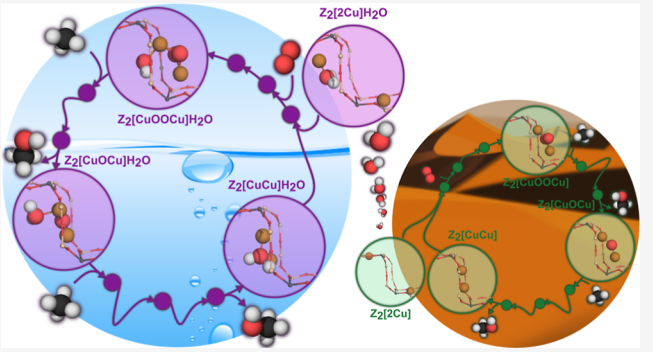

INTRODUCTION

Fossil fuels are currently the largest energy source, covering a third of the world's total energy consumption.[1] Finding alternatives to fossil fuels has become crucial as climate-neutral regulations are adopted worldwide that demand marginalization of fossil energy sources. Methanol is a renewable alternative to liquid fossil fuels, and zero net emissions can be achieved if methanol is produced from biomethane, which is a fermentation product. The current method to produce methanol from methane is, however, a multistep industrial-scale synthesis process that requires high temperature and high pressure. An appealing alternative is direct conversion in one step via the partial oxidation of methane

$$2CH_4 + O_2 \rightarrow 2CH_3OH \quad (1)$$

The challenge is, however, to avoid overoxidation of the thermodynamically preferred products CO and CO_2.

Direct conversion of methane into methanol is performed in nature via enzymatic methane monooxygenases (MMOs),[2,3] where partial oxidation of methane over the copper atoms in membrane-bound enzyme pMMO is one example.[3] Interestingly, the porous structure and ionic metal sites of the naturally occurring MMOs can also be found in ion-exchanged zeolites, which are porous aluminum silicates. Several different types of zeolites have been investigated for direct methane-to-methanol synthesis, of which some have shown promising results.[4−11] However, the atomic structures and mechanisms responsible for the activity of ion-exchanged zeolites are still debated. It has been suggested that different zeolite structures stabilize different sizes of the metal site. Copper trimers have, for example, been observed in large-pore structures, such as MFI and MOR[12] whereas monomers[13] and dimers[14] predominantly have been observed in small-pore zeolites, such as chabazite (CHA). In addition to the pore size, the number of Cu atoms in the preferred site is believed to be affected by the Si/Al ratio[15] and the distance between the Al ions in the zeolite framework.[16,17] The zeolite is at standard conditions humid, and the presence of water has been reported to affect the oxidation properties of the metal site[18,19] as well as the mechanism for methane-to-methanol conversion.[20,21] Using density functional theory (DFT) calculations in combination

Received: October 5, 2023
Revised: February 2, 2024
Accepted: February 12, 2024
Published: February 22, 2024

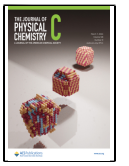

https://doi.org/10.1021/acs.jpcc.3c06635
J. Phys. Chem. C 2024, 128, 3641−3651

with kinetic modeling, we have shown that the presence of water significantly increases the activity of the Cu dimer site in the CHA framework, by increasing the mobility of the Cu cations, lowering reaction barriers, and facilitating the desorption of methanol.[22]

A crucial property of the catalytic site is its ability to change the oxidation state, which is required to adsorb O_2. Adsorption involves charge transfer from the Cu site to O_2 and the concurrent change in the oxidation state Cu(I) ↔ Cu(II). Other metals with the ability to change the oxidation state, such as Fe, are also potential candidates to catalyze direct methane-to-methanol conversion. In nature, a second version of the MMO enzyme is sMMO, which performs partial oxidation of methane with O_2 over an iron dimer.[3] In zeolites and with H_2O_2 as oxidant, Fe-Cu-ZSM-5 has shown the ability to partially oxidize methane under aqueous conditions.[20] The iron dimer structure is, in this case, believed to be responsible for the activity whereas copper inhibits overoxidation.[20] Other transition-metal atom of potential interest is Au and Pd. Using a mixture of H_2O_2 and O_2, an aqueous Au/Pd colloid, has shown high selectivity toward methanol in methane oxidation.[23] It is suggested that the dissociation of H_2O_2 activates CH_4, which then incorporates oxygen via the methyl radical. Direct methane-to-methanol formation (using H_2O_2) over Pd/Au surfaces suggests that alloying the surface reduces the barriers of the methanol formation.[24]

Here, we use first-principles calculations to investigate whether the reaction mechanism identified for Cu is viable for other transition mono- and bi-metallic dimers composed of Ag, Au, Pd, Ni, Co, Fe, and/or Zn. The identified partial oxidation reaction uses O_2 as oxidant and is explored over MeOOMe and MeOMe structures (with Me being a metal atom). The activity is investigated by using a microkinetic model calculating the turnover frequency (TOF) for a continuous reaction cycle. The influence of water on the reaction is studied by considering both dry and wet reaction conditions. We find that Cu_2, AuPd, and PdCu dimers have promising TOFs.

COMPUTATIONAL METHOD

DFT calculations were performed using the Vienna ab initio simulation package (VASP)[25−30] where the projector augmented wave method[31,32] models the interaction between the valence electrons and the cores. Projector augmented wave potentials were used with the valence states H($1s^1$), O($2s^22p^4$), C($2s^22p^2$), Al($3s^23p^1$), Si($3s^23p^2$), Fe($3d^74s^1$), Co($3d^84s^1$), Ni($3d^94s^1$), Cu($3d^{10}4s^1$), Pd($4d^{10}5s^0$), Ag($4d^{10}5s^1$), and Au($5d^{10}6s^1$). The exchange−correlation interaction was treated using the vdW-DF-cx functional,[33−35] which includes van der Waals interactions into the exchange−correlation by taking nonlocal screening into account. The Kohn−Sham orbitals were represented using a plane-wave basis set with 480 eV as the cutoff energy. A Gaussian smearing of 0.05 eV was applied to the Fermi level discontinuity. The electronic energies were converged to 10^{-8} eV in the self-consistent loop, and ionic positions were considered to be relaxed when the largest atomic force in the system was smaller than 0.02 eV/Å. The Brillouin zone was sampled by using only the Γ-point. The gas-phase molecules were treated in a cubic box with sides of 10 Å. The calculations were performed spin-polarized. Global optimization of the intermediate states was performed by local relaxations (quasi-Newton and conjugate-gradient methods) from ab initio molecular dynamics trajectories with Cu as the transition metal. Intermediate states for Me = Ag, Au, Pd, Ni, Co, Fe, and Zn were identified by using local optimization starting at the optimum Cu structure. The transition states (TSs) were obtained using the climbing NEB method[36−38] as implemented in VASP. The spin state of the structure was allowed to change during the TS search.

Vibrational energies were calculated by constructing a Hessian matrix using atomic forces generated by 0.01 Å displacements of the considered atoms. Only the extra-framework atoms, i.e., active site and reactants, were included in the vibration analysis. Note that as a combined result of set force criterion and soft modes of the considered systems, some low-lying frequencies (including any negative modes) of the adsorbed reaction intermediate were set to 100 cm^{-1}. All intermediate states have been analyzed for charge distribution using the Bader analysis method implemented by the Henkelman group.[39−42]

The relative stability of the reaction intermediate states was compared by calculating the change in Gibbs free energy

$$\Delta G(T, \Delta\mu) = \Delta H - T\Delta S(T) \tag{2}$$

where T is the temperature. In eq 2, the change in enthalpy is approximated as the difference in total energy[43] given by

$$\Delta H \approx \Delta E = E_{Z_2[Cu_2O_xH_{y+4}C]} - E_{Z_2[Cu_2O_xH_y]} - E_{CH_4} \tag{3}$$

ΔS is the difference in entropy between the adsorbed and gas-phase state

$$\Delta S = S_{adsorbed} - S_{gas-phase} \tag{4}$$

The translational entropy of gas-phase water, methane, and methanol was calculated using the ideal gas approximation whereas all vibrations were calculated using the harmonic approximation.[44,45] Rotations were treated by the rigid motor model.[46] The entropy of gas-phase molecules in the zeolite is set by the confinement set by the zeolite pores.[47,48] As a consequence, the entropy is calculated according to

$$S^{zeo} = \frac{2}{3}(S^{gas}_{trans} + S^{gas}_{rot}) + S^{zeo}_{vib} \tag{5}$$

where, S^{gas}_{trans} and S^{gas}_{rot} are entropy contributions from the gas-phase translations and rotations of the molecule, respectively, and S^{zeo}_{vib} is the entropy contribution from the vibrational modes of the molecule inside the zeolite. Using eq 5 makes the initial and final states to be unbound molecules absorbed inside the zeolite.

Zeolite Framework. CHA is a small-pored zeolite consisting of 4, 6, and 8 membered rings. Considering the hexagonal unit cell of the CHA framework with 36 tetrahedral sites (see Figure S1), a Si/Al ratio of 18 was used and is denoted Z_2. Two transition-metal ions were introduced to compensate for the +2 charge in the Z_2 zeolite system. The oxidation state of each Me atom is +1 in the absence of adsorbates. The used Al configuration is the same as in refs 14 and 21, which was optimized with respect to the bare Cu dimer. However, other Al distributions can favor other reaction intermediates.[49] In the Supporting Information, the relative energy of the Ze_2[MeOMe] state (*O) with respect to Al configuration is shown in Figure S2.

Microkinetic Modeling. The kinetic performance of the methane-to-methanol reaction mechanism for each system was investigated using mean-field microkinetic models based on the respective reaction energy landscapes to form CH_3OH. We

https://doi.org/10.1021/acs.jpcc.3c06635
J. Phys. Chem. C 2024, 128, 3641−3651

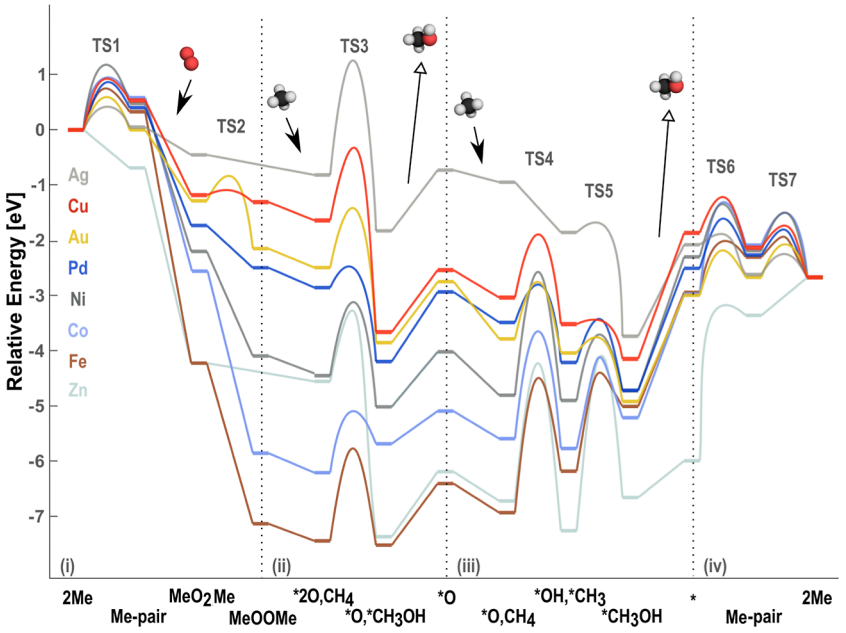

Figure 1. Reaction energy landscape for different transition-metal atoms during dry conditions. (i) Activation of O_2 by the Z_2[2Me] system. (ii) Partial oxidation of CH_4 over Z_2[MeOOMe]. (iii) Partial oxidation of CH_4 over Z_2[MeOMe]. (iv) Regeneration of the initial 2Me structure. Atom color codes: oxygen (red), hydrogen (white), and carbon (black).

did not consider formation of other possible reaction products such as dimethyl ether, CO, and CO_2.[50,51] Similar to our previous work,[22] the microkinetic model was formulated with elementary adsorption, desorption, and reaction steps accounting for each minimum in the reaction energy landscape. For the reaction steps, the forward rate constants were evaluated from transition state theory (TST)[46]

$$k_{TST} = \frac{k_B T}{h}\frac{Q'^{\ddagger}}{Q}\exp\left(-\frac{\Delta E}{k_B T}\right) = \frac{k_B T}{h}\exp\left(-\frac{\Delta G}{k_B T}\right) \quad (6)$$

where ΔE is the energy difference between initial state and TS, Q is the partition function for the initial state, $Q'^{\ddagger}$ is the partition function for the TS with the reaction coordinate excluded, k_B is Boltzmann's constant, and h is Planck's constant.

Adsorption was assumed to be barrierless, with the rate constants for oxygen, methane, and methanol adsorption calculated as

$$k_{ads} = \frac{pA}{(2\pi m k_B T)^{1/2}} \quad (7)$$

where p is the partial pressure of the molecule in the gas phase, A is the cross-sectional area of the pore consistent with similar studies,[52,53] and m is the mass of the molecule.

The rate constants for the reverse reaction steps and desorption were for thermodynamic consistency obtained through the equilibrium constant

$$K_{eq} = \frac{k_{ads}}{k_{des}} = \exp\left(-\frac{\Delta G}{k_B T}\right) \quad (8)$$

The differential equations describing the surface kinetics were solved using the Python Catalysis Kinetics (PyCatKin) tool,[54] using the SciPy[55] lsoda wrapper to the Fortran ODEPACK library,[56] and backward differentiation formulas. The relative and absolute tolerances were set to 1×10^{-8} and 1×10^{-10}, respectively. Steady states were checked using the nonlinear least-squares solver in SciPy, with the trust region reflective method,[57] and function and step-size tolerances of 1×10^{-8}. The analytical Jacobian function was provided to both solvers.

Scaling Relations. Linear scaling relations were fitted to describe the relative energy of each state in terms of the relative energy of the Z_2[MeOMe] state (*O). Separate scaling relations were derived for dry and wet conditions.

RESULTS AND DISCUSSION

The complete reaction cycle for the partial oxidation of methane-to-methanol is explored. For simplicity, the complete cycle is divided into four parts, (i) the activation of O_2, in which metal dimers as formed from two separate metal ions and O_2 are adsorbed, (ii) the adsorption and reaction of the first CH_4 with dioxygen to form methanol, (iii) the adsorption and reaction of the second CH_4 with the remaining oxygen to form the second methanol molecule, and finally (iv) the regeneration of the separate metal ions.

We use two different notations in the description of intermediate steps in the reaction energy landscape; one for the activation phase and one for the remaining three phases. The notation for the activation phase indicates the structure of the metal ions. For the remaining phases, the notation focuses on the composition of the metal site; thus, the two metal ions located in the 8MR are denoted *. The case with intermediate X chemisorbed to the metal ions and intermediate Y only weakly coordinated to the metal ions is, hence, denoted *X,Y.

Reaction Cycle during Dry Conditions. The reaction energy landscapes over Z_2[2Me]/Z_2[MeOOMe]/Z_2[MeOMe] with Me = Ag, Cu, Au, Pd, Ni, Co, Fe, and Zn are shown in Figure 1. See Figures S2 and S3 for an overview of the different structures involved in the reaction energy landscape under dry and wet conditions, respectively.

The first TS in the activation phase (i) is the diffusion of one of the metal atoms along the zeolite framework, moving the

https://doi.org/10.1021/acs.jpcc.3c06635
J. Phys. Chem. C 2024, 128, 3641−3651

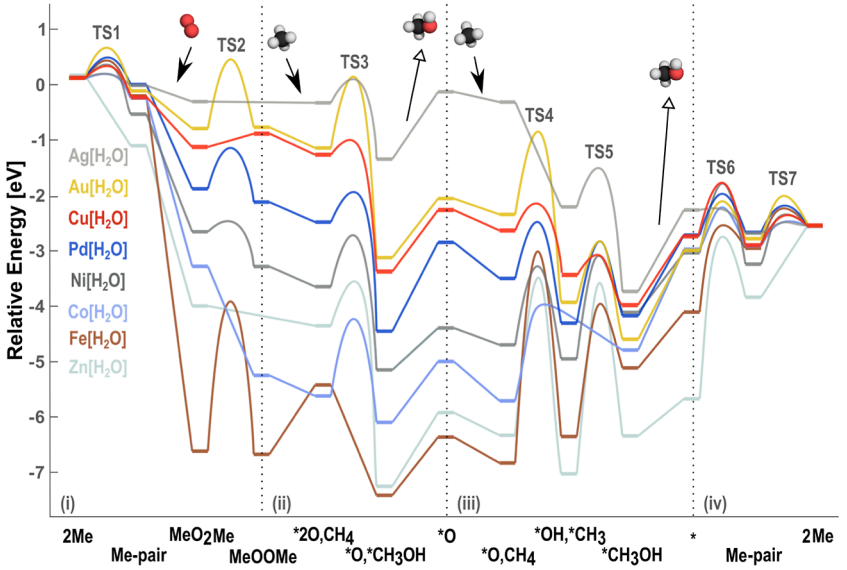

Figure 2. Reaction energy landscape during wet conditions. (i) Activation of O_2 by the Z_2[2Me] system. (ii) Partial oxidation of CH_4 over Z_2[MeOOMe]. (iii) Partial oxidation of CH_4 over Z_2[MeOMe]. (iv) Regeneration of the initial 2Me structure. Atom color code: oxygen (red), hydrogen (white), and carbon (black).

atom from the 6MR to the 8MR. All metals, with the exception of Zn, have a barrier for diffusion. The height varies from 0.42 eV for Ag to 1.18 eV for Ni. Adsorption of the compound on aqueous O_2 is assumed to occur without a barrier. In the structure MeO_2Me, Co and Ni have a Me−O distance of ∼1.7 Å; for Cu and Zn, the Me−O distance is ∼1.8 Å; for Au, Pd, and Fe the Me−O distance is ∼1.9 Å; and for Ag−O is ∼2.2 Å. The transformation of MeO_2Me to MeOOMe is for Cu and Au associated with a barrier of 0.09 and 0.45 eV, respectively, whereas the barriers to dissociate O_2 on Fe, Co, Ni, and Pd are negligible. No stable AgOOAg and ZnOOZn structures are identified and thus the reaction mechanism over Ag and Zn differs from that of the other metals. Fe, Co, and Ni form very stable MeOOMe structures with formation energies of 7.13, 5.85, and 4.12 eV, respectively. The longest Me−O distance in the MeOOMe configuration is calculated to be ∼1.9 Å for Au. For Pd, the distance is ∼1.8 Å, and for Fe, Ni, and Co it is ∼1.7 Å. The Me−Me distance is the longest for Cu with ∼3.4 Å, and the second longest for Au is ∼2.9 Å. Pd and Ni have a Me−Me distance of ∼2.5 Å, and Fe has the shortest distance (∼2.4 Å).

The second phase (ii) in the reaction energy landscape is CH_4 adsorption. CH_3OH formation over MeOOMe for Cu, Au, Pd, Fe, Ni, Co, AgO_2Ag, and ZnO_2Zn proceeds via the formation of a methyl radical (TS3). The lowest barrier for TS3 is calculated for Pd (0.78 eV) and the highest for Ag (1.77 eV). The desorption energy of the first CH_3OH molecule is low from Fe (0.41 eV) whereas it is high from Co (1.48 eV). Phase (iii) starts with CH_4 adsorption on intermediate state *O followed by two TSs; TS4 forms the methyl radical and TS5, which couples the OH and CH_3 groups. The lowest barrier for TS4 is calculated for Pd (0.70 eV) and the highest is for Zn (2.45 eV). The formation of the radical structure is barrierless over Ag. The barrier for methanol formation (TS5) is lowest for Cu (0.07 eV) and highest for Zn (3.23 eV). The lowest CH_3OH desorption energy is calculated for Zn (0.66 eV) and the highest for Ni (2.41 eV). The last phase (iv) is the regeneration of the original 2Me structure. The regeneration is associated with a barrier (TS6), which is the lowest for Ag (0.19 eV) and highest for Zn (2.82 eV). The last step in the reaction energy landscape is the diffusion of one metal atom from 8MR to 6MR (TS7), which is the reverse of TS1.

Overall, we find that Pd and Au have a reaction energy landscape that resembles that of Cu. Pd, however, has lower barriers for the activation phase (i), and Au has lower barriers during the formation of the first CH_3OH molecule (ii). As Zn, Fe, Ni, and Co form very stable intermediates, particularly $*2O,CH_4$, the possibility of completing the full reaction cycle over these sites is limited. Note that Ag does not follow the same intermediate steps as the reaction over Cu, which could be associated with the inability of Ag to adopt an oxidation state higher than Ag^{1+}.

During the reaction outlined in Figure 1, the spin state of the intermediates and TS change (as shown in Table S2), i.e., there is a crossing of the high-spin and the low-spin potential energy paths along the reaction coordinate. An example of this, the potential energy surface of CuO_2Cu (triplet) transformation to CuOOCu (singlet), together with spin-constrained calculation of the same transformation but fixed in the triplet and singlet state, respectively, is shown in Figure S3. Similar results are found in the literature, for instance see Shiota and Yoshizawa,[58] Chen et al.[59] The electronic process involved in the spin−flip can affect the reaction; thus, all rates calculated for the reaction should be considered an upper limit. Understanding the spin−flip process along the reaction coordinate is important; however, it is beyond the scope of this study. The charge distribution of the metal ions in each intermediate state is found in Tables S6−S13.

Reaction Cycle for Transition Metals during Wet Conditions. As zeolites are known to be humid, the introduction of H_2O into the reaction mechanism is important to simulate realistic conditions. Here, one H_2O is introduced into the mechanism and is allowed to interact with the reaction intermediates. It should be noted that the water molecule is included here in the role of a cocatalyst. The thermodynamic stability of one or more water molecules will depend on the reaction conditions;[49] thus, the results, e.g., TOF, might be restricted to certain external conditions. However, this lies outside the scope of this study. Figure 2 shows the resulting

https://doi.org/10.1021/acs.jpcc.3c06635
J. Phys. Chem. C 2024, 128, 3641−3651

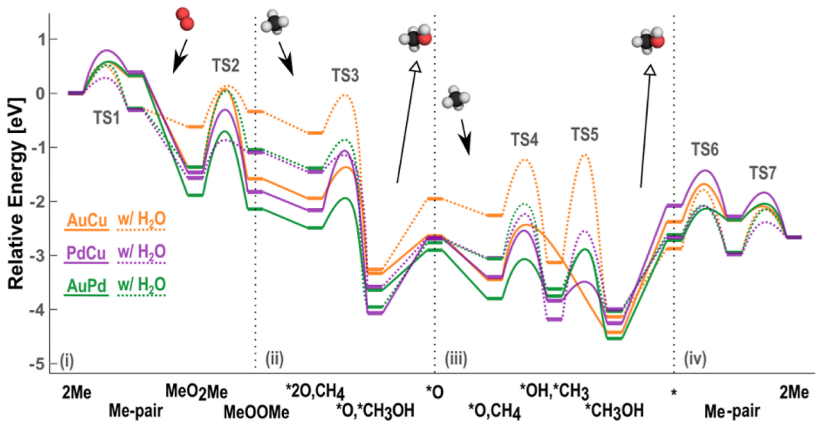

Figure 3. Reaction energy landscape for the bimetallic dimers AuCu, PdCu, and AuPd. The dry reaction conditions are shown in solid lines, and the conditions including one H_2O molecule are shown with dashed lines. (i) Activation of O_2 by the Z_2[2Me] system. (ii) Partial oxidation of CH_4 over Z_2[MeOOMe]. (iii) Partial oxidation of CH_4 over Z_2[MeOMe]. (iv) Regeneration of the initial 2Me structure. Atom color code: oxygen (red), hydrogen (white), and carbon (black).

reaction energy landscape. The different systems respond differently when H_2O is added to the mechanism. H_2O coordinates preferably to one of the metal atoms with an average adsorption energy of −0.99 eV. The lowest adsorption energy is calculated for Co (−0.53 eV) and the highest for Fe (−1.39 eV).

During activation phase (i), diffusion of the metal atoms along the zeolite framework (TS1) is facilitated for all elements in the presence of H_2O. Here, Ag and Co exhibit barriers of only 0.06 eV. The highest barrier for TS1 is associated with Au (0.53 eV). The most significant effect, when compared with dry conditions, is that of Co, where the barrier decreases with 1.12 eV whereas the effect is only minor for Au. The barrier in TS2 is lowered for Cu and Co when water is added, whereas the barriers for the other metals are increased. The largest change is calculated for Fe where the barrier increases by 2.70 eV.

In phase (ii), Cu, Ag, and Pd have the lowest barriers for methyl radical formation (TS3) being 0.28, 0.43, and 0.54 eV, respectively. The highest barrier is calculated for Fe (1.54 eV). The desorption energy of CH_3OH range from 0.54 eV (Co) to 1.60 eV (Pd). On the MeOMe[H_2O] structure, the average H_2O adsorption energy is 1.13 eV. The lowest adsorption energy is calculated for Ag (0.57 eV) and the highest for Co (1.66 eV). The Me−O distance can be grouped in three categories: ∼1.9 Å (Au, Ag, and Pd), ∼1.8 Å (Fe and Zn), and ∼1.7 Å (Ni and Co). Considering the Me−Me distance, the longest is calculated for Zn with ∼2.8 Å; Ag, Au, and Pd have ∼2.5 Å; Fe and Co ∼ 2.4 Å; and Ni ∼ 2.3 Å.

In phase (iii), the lowest barrier for TS4 is calculated for Cu (0.94 eV) and the highest barrier for Fe (3.85 eV). TS4 proceeds without a barrier for Ag. The lowest barrier for TS5 is again calculated for Cu (0.35 eV), and the highest TS5 barrier is obtained for Zn (3.40 eV). The Co system does not have any TS5. The lowest desorption energy of CH_3OH is in phase (iii) calculated for Zn (0.65 eV) and the highest for Au (1.60 eV).

In phase (iv), restructuring the active site from *[H_2O] is associated with a barrier in the range of 0.75 (Pd) to 2.84 eV (Zn). Restructuring occurs without a barrier for Ag.

As for the dry reaction mechanism, the spin states change during the wet reaction paths as outlined in Figure 2 (as shown in Table S2), and again, the rate calculated for the reaction should be considered an upper limit. The charge distribution of the metal ions in each intermediate state is found in Tables S6 to S13.

Reaction Cycle for Bimetallic Dimers. Based on the potential energy landscapes in Figures 1 and 2, the elements with the most promising reaction energy profiles for the methane-to-methanol reaction are Cu, Pd, and Au. The reactivity of the Pd intermediate states, the low CH_3OH desorption energies, low barriers for diffusion along the zeolite framework of Cu, and the partial inactivity of Au make these elements potential candidates for bimetallic combinations. The reaction energy landscapes for AuCu, PdCu, and AuPd are shown in Figure 3.

Reaction under Dry Conditions. The steps related to O_2 activation and especially TS2 are associated with higher barriers as compared to the single-metal systems. The lowest barrier (PdCu) is 0.72 eV higher than that for 2Au, which is the highest TS2 among the monometallic systems. The CH_4 activation barriers over the bimetallic dimers are instead lower than for the monometallic 2Cu and 2Au. The CH_3OH desorption energy is also lower over the bimetallic systems than that over the monometallic cases. The desorption energy for the first CH_3OH molecule is lowest for AuCu followed by AuPd. For the second CH_3OH, the desorption energy is lowest from AuPd, followed by that from the 2Au system. The lowest barrier for regeneration of the bimetallic structure is calculated for AuPd (0.58 eV). The AuPd dimer is the only system that does not display changes in the spin state during the reaction (Table S2).

Reaction under Wet Conditions. The bimetallic dimers consist of elements with different affinities toward water adsorption; however, there is a preference for H_2O to bind to Au, followed by Cu. In the 2Me[H_2O] state (separated metal cations), H_2O is adsorbed on Au in AuPd[H_2O] and AuCu[H_2O] with an adsorption energy of about 1.6 eV for both systems. H_2O is preferably adsorbed on Cu in the case of PdCu[H_2O] with an adsorption energy of 1.0 eV. TS1 is lowered for all bimetallic systems in the presence of water, and the first intermediate, Me-pair, is stabilized with an adsorption energy of 0.59 eV as compared to the dry case; see Figure 3. Adsorption of O_2 is destabilized in the presence of water, especially in the case of AuCu[H_2O]; and TS2 is consistently lower in the presence of water. The calculated adsorption

https://doi.org/10.1021/acs.jpcc.3c06635
J. Phys. Chem. C 2024, 128, 3641−3651

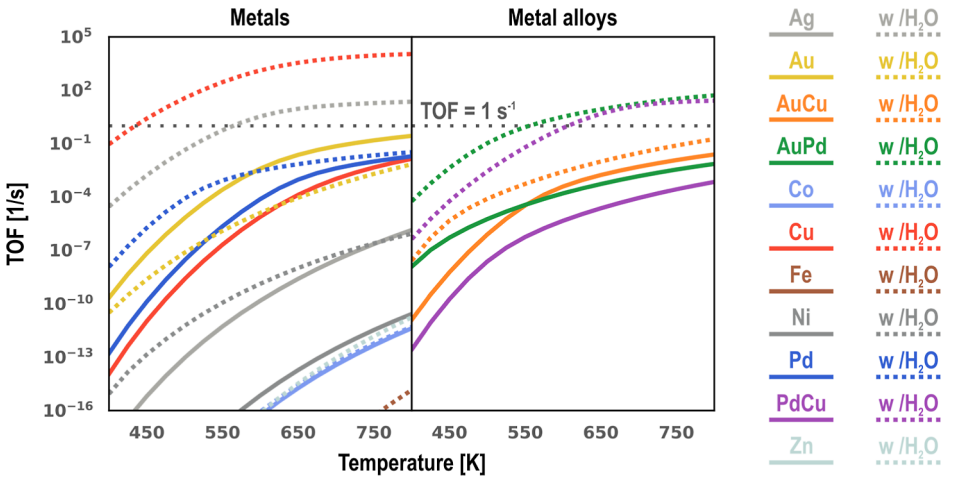

Figure 4. TOF predicted by the microkinetic model as a function of temperature for the dry (solid lines) and wet (dashed lines) metal (left) and metal alloy (right) systems.

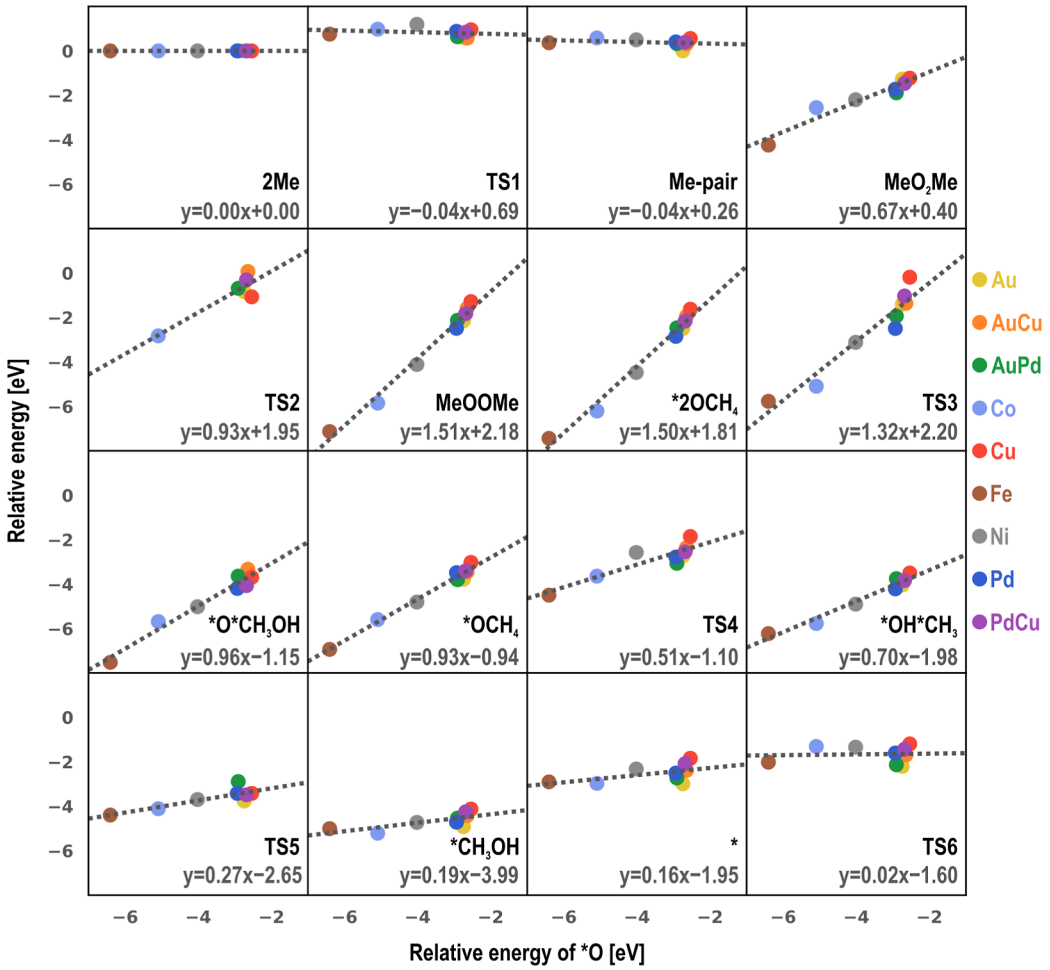

Figure 5. Relative energies of each state in the dry mechanism as a function of the relative energy of the *O state. Dotted lines show linear fits, with equations given in the lower right (details about the fits are provided in Table 1).

energy of the MeOOMe structure for PdCu[H_2O] is 0.30 eV, AuPd[H_2O] is 0.52 eV, and AuCu[H_2O] is 0.37 eV, which is 0.73, 1.10, and 1.25 eV lower than compared to the dry case, respectively. There is only a minor change in the adsorption energy of methane in the presence of water; however, the barrier during phase (ii), TS3, is affected in the case of PdCu[H_2O] and AuPd[H_2O]. In particular, the barrier for PdCu[H_2O] is 0.31 eV, which is decreased by 0.80 eV compared to the dry case. The desorption energy of the first CH_3OH is calculated to be 0.89 eV for PdCu[H_2O], 1.19 eV for AuPd[H_2O], and 1.30 eV for AuCu[H_2O]. Compared to the dry case, the Au-alloyed systems have an increase in the desorption energy, whereas PdCu[H_2O] is slightly destabilized. In the *O state, the AuCu[H_2O] has the largest

https://doi.org/10.1021/acs.jpcc.3c06635
J. Phys. Chem. C 2024, 128, 3641−3651

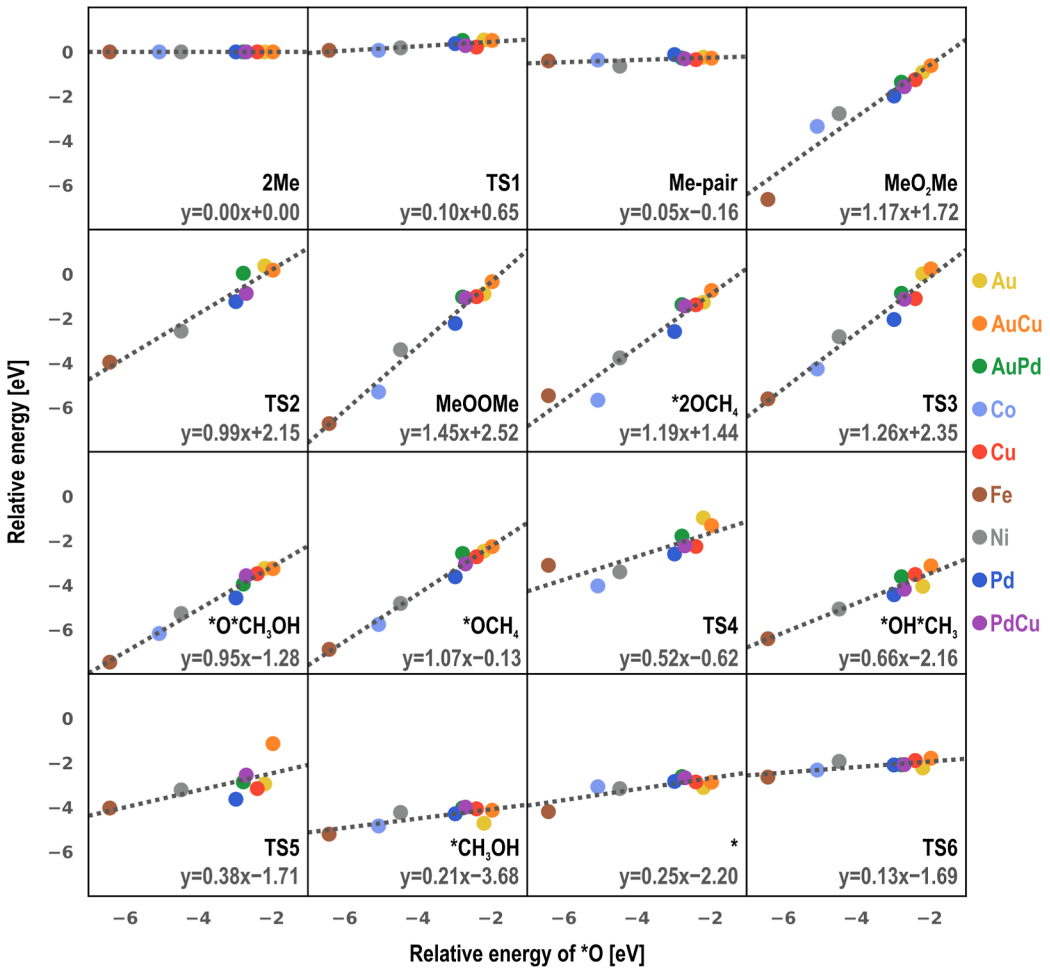

Figure 6. Relative energies of each state in the wet mechanism as a function of the relative energy of the *O state. Dotted lines show linear fits, with equations given in the lower right (details about the fits are provided in Table 2).

Table 1. Scaling Relations for Intermediates and TSs in the Dry System with 95% Confidence Intervals and Error Estimates

state	gradient	intercept	R^2	MAE (eV)	MAX (eV)
2Me	0.00 ± 0.00	0.00	0.00	0.00	0.00
TS1	−0.04 ± 0.13	0.69	0.06	0.17	0.35
Me-pair	−0.04 ± 0.11	0.26	0.08	0.12	0.35
MeO_2Me	0.67 ± 0.17	0.40	0.93	0.19	0.48
TS2	0.93 ± 0.59	1.95	0.83	0.30	0.65
MeOOMe	1.51 ± 0.18	2.18	0.98	0.23	0.36
$*2OCH_4$	1.50 ± 0.18	1.81	0.98	0.24	0.37
TS3	1.32 ± 0.36	2.20	0.92	0.40	0.96
$*O*CH_3OH$	0.96 ± 0.18	−1.15	0.96	0.22	0.35
$*OCH_4$	0.93 ± 0.12	−0.94	0.98	0.14	0.29
TS4	0.51 ± 0.23	−1.10	0.80	0.27	0.56
$*OH*CH_3$	0.70 ± 0.15	−1.98	0.96	0.18	0.25
TS5	0.27 ± 0.18	−2.65	0.69	0.16	0.55
$*CH_3OH$	0.19 ± 0.16	−3.99	0.53	0.19	0.41
*	0.16 ± 0.23	−1.95	0.29	0.26	0.60
TS6	0.02 ± 0.25	−1.60	0.00	0.31	0.56

destabilization, changing its relative energy with 0.68 eV, as compared to $AuPd[H_2O]$ where the relative energy is changed with 0.14 eV, and $PdCu[H_2O]$, which is unaffected. The barrier at T4 is marginally higher, whereas that at T5 is much higher (except for $AuPd[H_2O]$) when water is included. The desorption of the second CH_3OH is facilitated by water for all alloys, decreasing with 0.07, 0.30, and 0.56 eV for AuCu, AuPd, and PdCu, respectively. As for the dry reaction mechanism, the alloy of Au and Pd is the only site that does not have any change in the spin state during the reaction (Table S5).

Simulations of Reaction Kinetics. To study the implications of the reaction energy landscapes, we constructed mean-field microkinetic models for each system. A sequence of elementary reaction steps is defined based on the obtained

https://doi.org/10.1021/acs.jpcc.3c06635
J. Phys. Chem. C 2024, 128, 3641−3651

Table 2. Scaling Relations for Intermediates and TSs in the Wet System with 95% Confidence Intervals and Error Estimates

state	gradient	intercept	R^2	MAE (eV)	MAX (eV)
2Me	0.00 ± 0.00	0.00	0.00	0.00	0.00
TS1	0.10 ± 0.06	0.65	0.67	0.09	0.20
Me-pair	0.05 ± 0.07	−0.16	0.29	0.08	0.26
MeO_2Me	1.17 ± 0.30	1.72	0.92	0.37	0.89
TS2	0.99 ± 0.30	2.15	0.93	0.34	0.62
MeOOMe	1.45 ± 0.22	2.52	0.97	0.29	0.54
$*2OCH_4$	1.19 ± 0.32	1.44	0.92	0.38	1.10
TS3	1.26 ± 0.23	2.35	0.96	0.34	0.67
$*O*CH_3OH$	0.95 ± 0.13	−1.28	0.98	0.16	0.46
$*OCH_4$	1.07 ± 0.14	−0.13	0.98	0.15	0.51
TS4	0.52 ± 0.34	−0.62	0.65	0.50	0.87
$*OH*CH_3$	0.66 ± 0.20	−2.16	0.91	0.25	0.45
TS5	0.38 ± 0.43	−1.71	0.44	0.46	1.32
$*CH_3OH$	0.21 ± 0.17	−3.68	0.55	0.21	0.59
*	0.25 ± 0.16	−2.20	0.64	0.24	0.42
TS6	0.13 ± 0.10	−1.69	0.56	0.12	0.31

intermediates and TSs, starting with the metal cation pair in the 2Me configuration; see Figures S4 and S5. The steady-state TOF for methanol formation is obtained for all systems (Figure 4). As in our previous study,[22] we found that the presence of water significantly accelerated the kinetics of monometallic copper, which could achieve a reasonable TOF at 450 K. This is also the case for monometallic silver, palladium, and the three bimetallic systems. The opposite effect is observed for monometallic gold, where the dry system has a 1−2 orders of magnitude higher TOF. Increasing the temperatures, the AuPd dimer with H_2O is the first system after 2Cu to exceed a TOF of 1 s^{-1}, at a temperature of roughly 550 K, followed by 2Ag and PdCu. Note that the use of TOF equal to 1 s^{-1} is arbitrary; however, here, it is used as a measure of a relevant catalytic activity. The cobalt and nickel systems show low activity under both conditions, and the TOF is low also for the iron and dry zinc systems, for which stable intermediates hinder the performance. Thus, these systems are not active for methanol formation.

To investigate the trends in the kinetics across the different metal and metal alloy systems, we form linear scaling relations based on the binding energy of oxygen, i.e., between the relative energies of each state on the reaction energy landscape and the relative energy of the *O state. The *O state is chosen as it is anticipated to be a good descriptor for oxygen-bound states and by inspection of the reaction energy landscapes for all systems (Figures 1−3), which indicate a consistent trend for this intermediate. Figure 5 shows the fits for the dry case and Figure 6 shows the corresponding wet case. In both cases, 2Ag and 2Zn are excluded from the fit, owing to the significant differences in their electronic structures and reaction energy landscapes. Metrics describing the goodness of fit are provided in Table 1 for the dry conditions and Table 2 for the wet conditions. The mean absolute error (MAE) indicates how far the data lies from the scaling relation on average, and the range of values is between 0.08 and 0.46 eV. The maximum absolute error (MAX) highlights the largest discrepancies for each state, and the values range between 0.20 and 1.32 eV. These extremes both occur under wet conditions, with the smallest errors for Me-pair/TS1 and the largest for TS5, where AuCu lies highest above the scaling realtion.

The scaling relations describing the initial and final states (2ME, TS1, Me-pair, *, and TS6) are flat, which is expected because they do not involve oxygen, so its adsorption energy is not a good descriptor. The intercepts for 2ME, TS1, Me-pair, *, and TS6 describe the offset from the initial reference state. For the other states, under dry conditions, we observe that the slopes for MeO_2Me, TS4, and $*OH*CH_3$ are smaller than 1, whereas those of TS2, $*O*CH_3OH$ and $*OCH_4$ are close to 1. The slopes of MeOOMe and $*2OCH_4$ are around 1.5, and that of TS3 lies in-between 1 and 1.5. This can be rationalized by considering the configuration of atoms around the active site in these groups of systems relative to that of the descriptor. In the descriptor, the single oxygen atom is bound to two metal atoms, while in MeO_2Me, $*O*CH_3OH$, $*OH*CH_3$ and TS4, oxygen is interacting with an additional hydrogen/carbon and/or one of the metal−oxygen interactions are replaced with O−O/C−O. Thus, one might expect that these slopes are smaller than 1. By contrast, in MeOOMe and $*2OCH_4$, the two metal atoms are both interacting with both oxygen atoms, leading to a stronger binding energy in terms of that of the descriptor. TS3 involves weakening the metal−oxygen interaction in favor of oxygen−carbon interaction; thus, its slope is in between the gradients of those scaling relations. The slopes of the scaling relations for TS5 and $*CH_3OH$ are significantly less than 0.5. These states are relatively poorly defined by the scaling relation (Table 1), which is a consequence of the fact that the descriptor does not include the Me−C interaction. A similar state-wise analysis can be conducted under wet conditions with only minor differences. MeO_2Me has a slope close to 1, owing to the additional Me−O interaction introduced by the water, and $*2OCH_4$ has a slope also close to 1, due to water balancing the interaction with methane.

The scaling relations provide a more general model for the reaction energy landscape under dry and wet conditions. To investigate the kinetics across a range of possible systems, we used scaling relations to describe all reaction energies in the microkinetic model. The vibrational entropies of adsorbates in the AuPd system were used in the free energy calculations for all systems. AuPd was chosen because the wet AuPd system is the most active bimetallic system under all conditions. Figure 7 compares the TOF predicted by the scaling-relations-informed model across a range of *O energies to that of the first-principles-informed model for each metal and the metal alloy system. The trends in the scaling relation TOF volcano agree with the first-principles-based model under dry conditions: Au

https://doi.org/10.1021/acs.jpcc.3c06635
J. Phys. Chem. C 2024, 128, 3641−3651

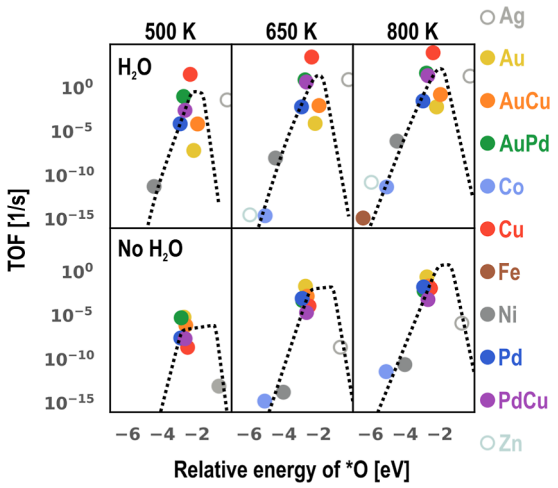

Figure 7. Comparison of kinetic predictions for the scaling relations (dashed line) and first-principles-based models (dots) under dry/wet conditions. Ag and Zn are shown unfilled as these systems were excluded from the scaling relation fitting.

lies near the apex and Co and Ni near the base. Under wet conditions, the peak in activity is obtained around the oxygen binding energies for Cu, AuPd, and PdCu; however, it is shifted toward slightly less negative values. Oxygen binding energies near those for Fe and Ni show similarly low activity. Under wet conditions, the scaling relation disagrees with the performance of systems with an oxygen binding energy near that of Ag, which is expected as the reaction energy landscape for Ag is very different. Three zones can be identified on the volcano, corresponding to strong, moderate, and weak oxygen adsorption energies. The slope of the volcano varies from positive, through flat, to negative, respectively, in these zones. The dominant intermediate differs in each zone (Figures S6 and S7), with adsorbed methane dominating in the strong adsorption zone, a combination of adsorbed methane and methanol in the moderate zone, and a combination of 2Me and Me-pair states observed in the weak zone.

CONCLUSIONS

The complete reaction mechanisms previously identified for the Cu dimer in CHA have been explored for other mono- and bi-metallic transition metal dimers, using first-principles calculations and microkinetic modeling, under dry and wet conditions. For the monometallic cases, all investigated metals, except Ag and Zn, have stable versions of the intermediate states optimized for Cu. The dimers of Fe, Ni, and Cu have a strong affinity for O_2 and form stable oxygen containing intermediates during the first oxidation cycle. Pd and Au are identified as the metals most likely to enhance the activity for direct methanol formation along a path similar to that of Cu under dry conditions. This is also observed in our first-principles-based microkinetic model, where the TOF is higher than for Cu for both Au (2−3 orders of magnitude) and Pd (1−0 orders of magnitude) in the temperature range of 400−800 K. However, it should be noted that the TOFs under dry conditions are low, thus rendering the candidates, under such conditions, less industrially relevant.

The intermediate states are generally destabilized by the addition of water to the reaction mixture over the monometallic dimers. However, the relative stability of the Fe, Zn, Ni, and Co intermediate states (as compared to Cu, Au, Ag, and Pd) is not changed, and the reaction remains unlikely over these metal dimers. The reaction energy landscape for Cu is positively affected by the addition of water, lowering all but one barrier and decreasing the desorption energy for CH_3OH. Water is lowers the barrier for migration of Pd and Ag along the zeolite, however, the barrier to form the methyl radical is increased. On Au, water increases the barriers but decreases the desorption energies. The effects of the change in the reaction energy landscape are reflected in the TOF. For instance, the TOF for Au is lowered by 1−3 orders of magnitude, whereas, for Cu and Ag, the TOF is increased by 2−10 and 4−9 orders of magnitude, respectively, across the temperature range of interest, thus rendering the candidates industrially relevant.

Alloying Cu, Au, and Pd gives the lowest barriers for the Au alloys during dry conditions and the Pd alloys during wet conditions. The positive effect of alloying is stronger under dry conditions. The potential energy diagram of PdCu is affected positively by the addition of water, whereas the energy diagram for AuCu is affected negatively. The AuPd dimer has the flattest overall reaction energy landscape of all of the alloy structures, both with and without water in the mechanism. For both dry and wet conditions, the alloying facilitates the activation of CH_4 and desorption of methanol. In particular, the TOF values of AuPd and PdCu under wet conditions are close to the value of Cu and are, thus, identified as promising candidates for direct methane-to-methanol conversion.

To gain further insights into the direct methane-to-methanol conversion, scaling relations of all reaction intermediates and TSs with respect to the adsorption energy of oxygen, *O, were developed. The scaling relations display a correlation of good quality to the descriptor as confirmed by using various metrics. Using the scaling relations as input to the microkinetic model, it is clear that the already identified candidates, i.e., 2Cu, AuPd, and PdCu, are close to the top of the volcano. The agreement indicates that the scaling reactions capture the most important features in the reaction landscape of the different elements. Excluding competing reaction paths, e.g., complete oxidation to CO_2, the candidates, 2Cu, AuPd, and PdCu, display a TOF sufficient to render them technologically relevant for direct methane-to-methanol conversion.

ASSOCIATED CONTENT

Supporting Information

The Supporting Information is available free of charge at https://pubs.acs.org/doi/10.1021/acs.jpcc.3c06635.

Zeolite structure, relative energy, enthalpy of formation, spin state analysis, charge analysis, and microkinetic model (PDF)

Structures (ZIP)

AUTHOR INFORMATION

Corresponding Author

Anders Hellman − *Department of Physics, Chalmers University of Technology, Göteborg SE 412 96, Sweden; Competence Centre for Catalysis, Chalmers University of Technology, Göteborg SE 412 96, Sweden;* orcid.org/0000-0002-1821-159X; Email: anders.hellman@chalmers.se

https://doi.org/10.1021/acs.jpcc.3c06635
J. Phys. Chem. C 2024, 128, 3641−3651

Authors

Unni Engedahl − *Department of Physics, Chalmers University of Technology, Göteborg SE 412 96, Sweden; Competence Centre for Catalysis, Chalmers University of Technology, Göteborg SE 412 96, Sweden;* orcid.org/0000-0002-1871-6010

Astrid Boje − *Department of Physics, Chalmers University of Technology, Göteborg SE 412 96, Sweden;* orcid.org/0000-0002-2487-0276

Henrik Ström − *Department of Mechanics and Maritime Sciences, Chalmers University of Technology, Göteborg SE 412 96, Sweden;* orcid.org/0000-0002-8581-5174

Henrik Grönbeck − *Department of Physics, Chalmers University of Technology, Göteborg SE 412 96, Sweden; Competence Centre for Catalysis, Chalmers University of Technology, Göteborg SE 412 96, Sweden;* orcid.org/0000-0002-8709-2889

Complete contact information is available at: https://pubs.acs.org/10.1021/acs.jpcc.3c06635

Notes

The authors declare no competing financial interest.

■ ACKNOWLEDGMENTS

Financial support was gratefully acknowledged from the Knut and Alice Wallenberg Foundation through the projects "Atomistic design of catalysts" (no.: KAW 2015.0058) and "Single particle catalysis in nanoreactors" (no.: KAW 2015.0057). The Competence Centre for Catalysis (KCK) is hosted by Chalmers University of Technology and is financially supported by the Swedish Energy Agency and the member companies Johnson Matthey, Perstorp, Powercell, Preem, Scania CV, Umicore, and Volvo Group. Calculations were performed at PDC (Stockholm) and NSC (Linköping) via a SNIC grant.

■ REFERENCES

(1) BP plc. *Statistical Review of World Energy 2020*; BP plc, 2020.

(2) Sirajuddin, S.; Rosenzweig, A. C. Enzymatic Oxidation of Methane. *Biochemistry* **2015**, *54*, 2283−2294.

(3) Ross, M.; Rosenzweig, A. A tale of two methane monooxygenases. *J. Biol. Inorg. Chem.* **2017**, *22*, 307−319.

(4) Wang, X.; Martin, N. M.; Nilsson, J.; Carlson, S.; Gustafson, J.; Skoglundh, M.; Carlsson, P.-A. Copper-Modified Zeolites and Silica for Conversion of Methane to Methanol. *Catalysts* **2018**, *8*, 545.

(5) Newton, M. A.; Knorpp, A. J.; Pinar, A. B.; Sushkevich, V. L.; Palagin, D.; van Bokhoven, J. A. On the Mechanism Underlying the Direct Conversion of Methane to Methanol by Copper Hosted in Zeolites; Braiding Cu K-Edge XANES and Reactivity Studies. *J. Am. Chem. Soc.* **2018**, *140*, 10090−10093.

(6) Li, G.; Vassilev, P.; Sanchez-Sanchez, M.; Lercher, J. A.; Hensen, E. J.; Pidko, E. A. Stability and reactivity of copper oxo-clusters in ZSM-5 zeolite for selective methane oxidation to methanol. *J. Catal.* **2016**, *338*, 305−312.

(7) Groothaert, M. H.; Smeets, P. J.; Sels, B. F.; Jacobs, P. A.; Schoonheydt, R. A. Selective Oxidation of Methane by the Bis(μ-oxo)dicopper Core Stabilized on ZSM-5 and Mordenite Zeolites. *J. Am. Chem. Soc.* **2005**, *127*, 1394−1395.

(8) Narsimhan, K.; Iyoki, K.; Dinh, K.; Román-Leshkov, Y. Catalytic Oxidation of Methane into Methanol over Copper-Exchanged Zeolites with Oxygen at Low Temperature. *ACS Cent. Sci.* **2016**, *2*, 424−429.

(9) Pappas, D. K.; Borfecchia, E.; Dyballa, M.; Pankin, I. A.; Lomachenko, K. A.; Martini, A.; Signorile, M.; Teketel, S.; Arstad, B.; Berlier, G.; et al. Methane to Methanol: Structure−Activity Relationships for Cu-CHA. *J. Am. Chem. Soc.* **2017**, *139*, 14961−14975.

(10) Kulkarni, A. R.; Zhao, Z.-J.; Siahrostami, S.; Nørskov, J. K.; Studt, F. Monocopper Active Site for Partial Methane Oxidation in Cu-Exchanged 8MR Zeolites. *ACS Catal.* **2016**, *6*, 6531−6536.

(11) Zhao, Z.-J.; Kulkarni, A.; Vilella, L.; Nørskov, J. K.; Studt, F. Theoretical Insights into the Selective Oxidation of Methane to Methanol in Copper-Exchanged Mordenite. *ACS Catal.* **2016**, *6*, 3760−3766.

(12) Mao, Y.; Hu, P. Identification of the active sites and mechanism for partial methane oxidation to methanol over copper-exchanged CHA zeolites. *Sci. China: Chem.* **2020**, *63*, 850−859.

(13) Paolucci, C.; Parekh, A. A.; Khurana, I.; Di Iorio, J. R.; Li, H.; Albarracin Caballero, J. D.; Shih, A. J.; Anggara, T.; Delgass, W. N.; Miller, J. T.; et al. Catalysis in a Cage: Condition-Dependent Speciation and Dynamics of Exchanged Cu Cations in SSZ-13 Zeolites. *J. Am. Chem. Soc.* **2016**, *138*, 6028−6048.

(14) Engedahl, U.; Grönbeck, H.; Hellman, A. First-Principles Study of Oxidation State and Coordination of Cu-Dimers in Cu-SSZ-13 during Methane-to-Methanol Reaction Conditions. *J. Phys. Chem. C* **2019**, *123*, 26145−26150.

(15) Ipek, B.; Wulfers, M. J.; Kim, H.; Göltl, F.; Hermans, I.; Smith, J. P.; Booksh, K. S.; Brown, C. M.; Lobo, R. F. Formation of [Cu2O2]2+ and [Cu2O]2+ toward C−H Bond Activation in Cu-SSZ-13 and Cu-SSZ-39. *ACS Catal.* **2017**, *7*, 4291−4303.

(16) Vilella, L.; Studt, F. The Stability of Copper Oxo Species in Zeolite Frameworks. *Eur. J. Inorg. Chem.* **2016**, *2016*, 1514−1520.

(17) Fant, M.; Ångqvist, M.; Hellman, A.; Erhart, P. To Every Rule There is an Exception: A Rational Extension of Loewenstein's Rule. *Angew. Chem.* **2021**, *133*, 5192−5195.

(18) Koishybay, A.; Shantz, D. F. Water Is the Oxygen Source for Methanol Produced in Partial Oxidation of Methane in a Flow Reactor over Cu-SSZ-13. *J. Am. Chem. Soc.* **2020**, *142*, 11962−11966.

(19) Sushkevich, V. L.; Palagin, D.; Ranocchiari, M.; van Bokhoven, J. A. Selective anaerobic oxidation of methane enables direct synthesis of methanol. *Am. Assoc. Adv. Sci.* **2017**, *356*, 523−527.

(20) Hammond, C.; Forde, M. M.; Ab Rahim, M. H.; Thetford, A.; He, Q.; Jenkins, R. L.; Dimitratos, N.; Lopez-Sanchez, J. A.; Dummer, N. F.; Murphy, D. M.; et al. Direct Catalytic Conversion of Methane to Methanol in an Aqueous Medium by using Copper-Promoted Fe-ZSM-5. *Angew. Chem., Int. Ed.* **2012**, *51*, 5129−5133.

(21) Engedahl, U.; Arvidsson, A. A.; Grönbeck, H.; Hellman, A. Reaction Mechanism for Methane-to-Methanol in Cu-SSZ-13: First-Principles Study of the Z2[Cu2O] and Z2[Cu2OH] Motifs. *Catalysts* **2021**, *11*, 17.

(22) Engedahl, U.; Boje, A.; Ström, H.; Grönbeck, H.; Hellman, A. Complete Reaction Cycle for Methane-to-Methanol Conversion over Cu-SSZ-13: First-Principles Calculations and Microkinetic Modeling. *J. Phys. Chem. C* **2021**, *125*, 14681−14688.

(23) Agarwal, N.; Freakley, S. J.; McVicker, R. U.; Althahban, S. M.; Dimitratos, N.; He, Q.; Morgan, D. J.; Jenkins, R. L.; Willock, D. J.; Taylor, S. H.; et al. Aqueous Au-Pd colloids catalyze selective CH4 oxidation to CH3OH with O2 under mild conditions. *Science* **2017**, *358*, 223−227.

(24) Sajith, P. K.; Staykov, A.; Yoshida, M.; Shiota, Y.; Yoshizawa, K. Theoretical Study of the Direct Conversion of Methane to Methanol Using H2O2 as an Oxidant on Pd and Au/Pd Surfaces. *J. Phys. Chem. C* **2020**, *124*, 13231−13239.

(25) Kresse, G.; Hafner, J. Ab Initio molecular dynamics for liquid metals. *Phys. Rev. B: Condens. Matter Mater. Phys.* **1993**, *47*, 558−561.

(26) Kresse, G.; Furthmüller, J. Efficiency of Ab-Initio Total Energy Calculations for Metals and Semiconductors Using a Plane-Wave Basis Set. *Comput. Mater. Sci.* **1996**, *6*, 15−50.

(27) Kresse, G.; Furthmüller, J. Efficient Iterative Schemes for Ab Initio Total-Energy Calculations Using a Plane-Wave Basis Set. *Phys. Rev. B: Condens. Matter Mater. Phys.* **1996**, *54*, 11169−11186.

(28) Kresse, G.; Hafner, J. Norm-conserving and ultrasoft pseudopotentials for first-row and transition elements. *J. Phys.: Condens. Matter* **1994**, *6*, 8245−8257.

(29) Klimes, J.; Bowler, D. R.; Michaelides, A. Chemical accuracy for the Van der Waals density functional. *J. Phys.: Condens.Matter* **2010**, *22*, 022201.
(30) Klimes, J.; Bowler, D. R.; Michaelides, A. Van der Waals density functionals applied to solids. *Phys. Rev. B: Condens. Matter Mater. Phys.* **2011**, *83*, 195131.
(31) Blöchl, P. E. Projector Augmented-Wave Method. *Phys. Rev. B: Condens. Matter Mater. Phys.* **1994**, *50*, 17953−17979.
(32) Kresse, G.; Joubert, D. From ultrasoft pseudopotentials to the projector augmented-wave method. *Phys. Rev. B: Condens. Matter Mater. Phys.* **1999**, *59*, 1758−1775.
(33) Dion, M.; Rydberg, H.; Schröder, E.; Langreth, D. C.; Lundqvist, B. I. Van der Waals Density Functional for General Geometries. *Phys. Rev. Lett.* **2004**, *92*, 246401.
(34) Lee, K.; Murray, E. D.; Kong, L.; Lundqvist, B. I.; Langreth, D. C. Higher-accuracy van der Waals density functional. *Phys. Rev. B: Condens. Matter Mater. Phys.* **2010**, *82*, 081101.
(35) Berland, K.; Hyldgaard, P. Exchange functional that tests the robustness of the plasmon description of the Van der Waals density functional. *Phys. Rev. B: Condens. Matter Mater. Phys.* **2014**, *89*, 035412.
(36) Sheppard, D.; Terrell, R.; Henkelman, G. Optimization methods for finding minimum energy paths. *J. Chem. Phys.* **2008**, *128*, 134106.
(37) Henkelman, G.; Jónsson, H. Improved tangent estimate in the nudged elastic band method for finding minimum energy paths and saddle points. *J. Chem. Phys.* **2000**, *113*, 9978−9985.
(38) Henkelman, G.; Uberuaga, B. P.; Jónsson, H. A climbing image nudged elastic band method for finding saddle points and minimum energy paths. *J. Chem. Phys.* **2000**, *113*, 9901−9904.
(39) Tang, W.; Sanville, E.; Henkelman, G. A grid-based Bader analysis algorithm without lattice bias. *J. Phys.: Condens. Matter* **2009**, *21*, 084204.
(40) Sanville, E.; Kenny, S.; Smith, R.; Henkelman, G. Improved grid-based algorithm for Bader charge allocation. *J. Comput. Chem.* **2007**, *28*, 899−908.
(41) Henkelman, G.; Arnaldsson, A.; Jónsson, H. A Fast and Robust Algorithm for Bader Decomposition of Charge Density. *Comput. Mater. Sci.* **2006**, *36*, 354−360.
(42) Yu, M.; Trinkle, D. Accurate and efficient algorithm for Bader charge integration. *J. Chem. Phys.* **2011**, *134*, 064111.
(43) Reuter, K.; Scheffler, M. Composition, structure, and stability of RuO_2(110) as a function of oxygen pressure. *Phys. Rev. B: Condens. Matter Mater. Phys.* **2001**, *65*, 035406.
(44) Hjorth Larsen, A.; Jørgen Mortensen, J.; Blomqvist, J.; Castelli, I. E.; Christensen, R.; Dułak, M.; Friis, J.; Groves, M. N.; Hammer, B.; Hargus, C.; et al. The atomic simulation environment—a Python library for working with atoms. *J. Phys.: Condens. Matter* **2017**, *29*, 273002.
(45) Bahn, S. R.; Jacobsen, K. W. An object-oriented scripting interface to a legacy electronic structure code. *Comput. Sci. Eng.* **2002**, *4*, 56−66.
(46) Chorkendorff, I.; Niemantsverdriet, J. W. *Concepts of Modern Catalysis and Kinetics*; John Wiley & Sons, 2006.
(47) Jørgensen, M.; Chen, L.; Grönbeck, H. Monte Carlo Potential Energy Sampling for Molecular Entropy in Zeolites. *J. Phys. Chem. C* **2018**, *122*, 20351−20357.
(48) Chen, L.; Janssens, T. V. W.; Vennestrøm, P. N. R.; Jansson, J.; Skoglundh, M.; Grönbeck, H. A Complete Multisite Reaction Mechanism for Low-Temperature NH3-SCR over Cu-CHA. *ACS Catal.* **2020**, *10*, 5646−5656.
(49) Göltl, F.; Bhandari, S.; Mavrikakis, M. Thermodynamics Perspective on the Stepwise Conversion of Methane to Methanol over Cu-Exchanged SSZ-13. *ACS Catal.* **2021**, *11*, 7719−7734.
(50) Dinh, K. T.; Sullivan, M. M.; Narsimhan, K.; Serna, P.; Meyer, R. J.; Dincă, M.; Román-Leshkov, Y. Continuous Partial Oxidation of Methane to Methanol Catalyzed by Diffusion-Paired Copper Dimers in Copper-Exchanged Zeolites. *J. Am. Chem. Soc.* **2019**, *141*, 11641−11650.
(51) Ipek, B.; Lobo, R. F. Catalytic Conversion of Methane to Methanol on Cu-SSZ-13 Using N_2O as Oxidant. *Chem. Commun.* **2016**, *52*, 13401−13404.
(52) Arvidsson, A. A.; Plessow, P. N.; Studt, F.; Hellman, A. Influence of Acidity on the Methanol-to-DME Reaction in Zeotypes: A First Principles-Based Microkinetic Study. *J. Phys. Chem. C* **2020**, *124*, 14658−14663.
(53) Horvatits, C.; Li, D.; Dupuis, M.; Kyriakidou, E. A.; Walker, E. A. Ethylene and water co-adsorption on Ag/SSZ-13 zeolites: a theoretical study. *J. Phys. Chem. C* **2020**, *124*, 7295−7306.
(54) Boje, A.; Ström, H.; Hellman, A. PyCatKin. 2021, https://github.com/aab64/PyCatKin (accessed Aug 02, 2022).
(55) Virtanen, P.; Gommers, R.; Oliphant, T. E.; Haberland, M.; Reddy, T.; Cournapeau, D.; Burovski, E.; Peterson, P.; Weckesser, W.; Bright, J.; et al. SciPy 1.0: Fundamental Algorithms for Scientific Computing in Python. *Nat. Methods* **2020**, *17*, 261−272.
(56) Hindmarsh, A. C. *ODEPACK, A Systematized Collection of ODE Solvers*; Scientific Computing: North-Holland, 1983; pp 55−64.
(57) Branch, M. A.; Coleman, T. F.; Li, Y. A Subspace, Interior, and Conjugate Gradient Method for Large-Scale Bound-Constrained Minimization Problems. *SIAM J. Sci. Comput.* **1999**, *21*, 1−23.
(58) Shiota, Y.; Yoshizawa, K. Methane-to-Methanol Conversion by First-Row Transition-Metal Oxide Ions:ScO+, TiO+, VO+, CrO+, MnO+, FeO+, CoO+, NiO+, and CuO+. *J. Am. Chem. Soc.* **2000**, *122*, 12317−12326.
(59) Chen, L.; Falsig, H.; Janssens, T. V. W.; Jansson, J.; Skoglundh, M.; Grönbeck, H. Effect of Al-distribution on oxygen activation over Cu−CHA. *Catal. Sci. Technol.* **2018**, *8*, 2131−2136.

https://doi.org/10.1021/acs.jpcc.3c06635
J. Phys. Chem. C 2024, 128, 3641−3651